Applied Radiation and Isotopes 224 (2025) 111942

Contents lists available at ScienceDirect

Applied Radiation and Isotopes

journal homepage: www.elsevier.com/locate/apradiso

Effect of Ce^{3+} doping on the structural, optical, and dosimetric properties of magnesium-borate glasses

Gerardo R. Barrera [a,b], Adriel S. Almeida [a], Bruno M. Vidigal [a], Anderson M.B. Silva [c], Matheus C.S. Nunes [d], Andrea L.F. Novais [e], Neilo M. Trindade [f], Divanizia N. Souza [a,*]

[a] Departamento de Física, Universidade Federal de Sergipe, São Cristovão, SE, Brazil
[b] Universidad Surcolombiana, USCO, Neiva, Huila, Colombia
[c] Instituto de Pesquisas Energéticas e Nucleares, Comissão Nacional de Energia Nuclear, São Paulo, Brazil
[d] Instituto de Ciência e Tecnologia, Universidade Estadual Paulista (UNESP), Sorocaba, SP, Brazil
[e] Faculdade de Engenharia Mecânica, Universidade Federal Do Sul e Sudeste Do Pará, Marabá, Pará, Brazil
[f] Instituto de Física, Universidade de São Paulo, São Paulo, Brazil

ARTICLE INFO

Keywords:
Magnesium-borate glasses
Ce^{3+} doping
Structural properties
Optical properties
Optically stimulated luminescence

ABSTRACT

Ce^{3+} doped magnesium-borate glasses with compositions $80MgB_2O_4$-$20MgB_4O_7$:xCe and $60MgB_2O_4$-$40MgB_4O_7$:xCe (where x = 0.10, 0.30, 0.50, 0.70, and 0.90 wt%), were successfully synthesized using the melt quenching method. The physical, structural, and luminescent properties of the glasses were systematically investigated through density measurements, X-ray diffraction (XRD), differential scanning calorimetry (DSC), optical absorption, spectrofluorometry, and optically stimulated luminescence (OSL). XRD patterns confirmed the amorphous nature of the glasses, while DSC provided insights into their thermal stability and phase transition behavior. The thermal stability of the 60 MBO matrix was found to be higher than that of the 80 MBO glass. An increase in glass density with higher Ce^{3+} concentrations was observed, accompanied by a reduction in molar volume. The indirect and direct optical band gap decreased with increasing Ce^{3+} content, correlating with the observed decrease in molar volume. Photoluminescence studies revealed emissions associated with Ce^{3+} ions incorporated into the glass matrix. Additionally, OSL measurements demonstrated the dose-response behavior of the glasses over the range of 0.02–5 Gy. Particularly, the 60MBO glass composition exhibited superior sensitivity to ionizing radiation compared to the 80MBO composition. The OSL signal of the 60MGO glass fades significantly within a few days. Long-term stability of the OSL signal should be a goal for new studies on these glasses.

1. Introduction

The search for new methods to produce solid materials has been an area of intense research in recent years (Feitosa, 2004). Both crystalline and amorphous materials have been considered due to their practical applications in various fields. In the context of radiation measurements, these materials are used to convert incident radiation into light, enabling its indirect detection by conventional photodetectors. Key applications include imaging detectors for radiodiagnostic (Rowlands, 2002), scintillators (Yanagida et al., 2022), and dosimeters (Okada et al., 2011). When a single photon of incident radiation ionizes the material, a released electron can create thousands of electron-hole pairs. Some of these charges recombine instantly, emitting scintillating light (Okada et al., 2016), while others become trapped in shallow or deep traps. These trapped charges can subsequently recombine at luminescent centers, emitting light through thermally stimulated luminescence (TSL) when the material is heated (McKeever, 1988) or through optically stimulated luminescence (OSL) when exposed to light (Yukihara and McKeever, 2011).

Borate glasses have been investigated for their promising properties, including excellent transparency, isotropic nature, easy handling, low fabrication costs, and flexible chemical compositions. These characteristics make borate glasses suitable for a wide range of applications in optics, electronics, biomedicine, and radiation dosimetry (Mhareb et al., 2015; Barrera et al., 2018; Silva et al., 2023). The incorporation of alkali and rare earth alkaline modifiers improves the material in its structural,

This article is part of a special issue entitled: Reprolam 2024 published in Applied Radiation and Isotopes.

* Corresponding author.
E-mail address: divanizia@gmail.com (D.N. Souza).

https://doi.org/10.1016/j.apradiso.2025.111942
Received 30 January 2025; Received in revised form 3 May 2025; Accepted 22 May 2025
Available online 24 May 2025

thermal, optical, and magnetic properties (Lim et al., 2014).

Rare-earth ions, particularly Ce^{3+}, have been widely used as activators in various fluoride and oxide materials due to their superior spectroscopic properties. Ce^{3+}-doped crystals and glasses exhibit high light yield and short luminescence decay time (Wantana et al., 2018; Kawano et al., 2018), making them highly attractive for optical applications. Ce^{3+} ions (4f1 electron configuration) emit efficiently in the UV–VIS spectral region with broad band emission due to 5d−4f allowed transitions (Kawano et al., 2018). The position of these transitions depends strongly on the host material's structure, as the crystal-field splits the 5d levels, leading to emission wavelengths that range from the near UV to the red-light region.

Cerium-doped glasses have demonstrated considerable potential in radiation measurements. These materials convert incident radiation into light, so that the radiation is indirectly detected using a conventional photodetector. Numerous Ce^{3+}-doped materials have shown dosimeter properties, including TSL and OSL. For instance, $Li_3PO4Al(PO_3)_3$ glass doped with different concentrations of Ce has been studied for its scintillator and dosimeter properties, showing a linear dose-response and suitability for high-dose radiotherapy (Tatsumi et al., 2016). Similarly, Ce-doped Sol-gel silica glass has demonstrated a linear OSL dose-response up to 500 Gy under X-ray irradiation, which makes it potentially suitable for dosimetry in harsh environments, even in the case of high-dose rate conditions (Al Helou et al., 2018).

In this work, two new magnesium-borate glasses, $80MgB_2O_4$-$20MgB_4O_7$:Ce and $60MgB_2O_4$-$40MgB_4O_7$:Ce, were synthesized and investigated. For simplicity, these materials are referred to as 80MBO and 60MBO, respectively. The structural, optical, and luminescence properties were investigated as a function of Ce^{3+} concentration. The OSL technique was used to investigate the dosimetric properties of these materials.

2. Materials and methods

2.1. Synthesis of glasses

The undoped and Ce-doped magnesium-borate glasses were synthesized using a mixture of magnesium tetraborate (MgB_4O_7) and diborate (MgB_2O_4). The precursor compounds, MgB_4O_7 and MgB_2O_4, were synthesized via solid-state synthesis, as described by Souza et al. (2015). Analytical grade MgO (Merck, 99.9 % purity) and H3BO3 (Merck, 99.9 % purity) were used for the preparation of MgB_4O_7 and MgB_2O_4. Cerium carbonate ($Ce_2(CO_3)3xH_2O$, Sigma-Aldrich, 99.9 % purity) was used as a dopant. The compositions of the glass systems were prepared as follows: 80 % MgB_2O_4–20 % MgB_4O_7:Ce_x and 60 % MgB_2O_4–40 % MgB_4O_7:Ce_x, with $0.0 < x < 1.0$ wt% (Table 1).

2.2. Glass preparation

The glasses were prepared using the melt-quenching technique. Reagent mixtures were heated in an alumina crucible at a rate of 30 °C/min and held at 1150 °C for 5 h to ensure complete melting. During this process, the melts were stirred to ensure homogeneity and then poured into aluminum molds (at room temperature) with dimensions of 6 mm in diameter, 2 mm deep, to form pellet-shaped samples. To relieve residual internal stress, the samples were held at 200 °C for 3 h during the molding process. Each pellet weighed approximately 50 mg. Fig. 1 shows the main steps of the analysis performed on the glass samples. It provides a visual summary of the experimental workflow.

2.3. Structural and thermal characterization

The vitreous structure of the samples was confirmed by X-ray diffraction (XRD) using a Bruker diffractometer with a tube operating at 40 kV/40 mA. Measurements were conducted with steps $2\theta\,(^\circ) = 0.5$ in a 2θ scan range of $10^\circ < 2\theta < 90^\circ$ with 10 s per step at room temperature. The glass and the crystal temperature points were performed using DSC analysis, Netzsch STA 449 F1 Jupiter equipment, with synthetic air atmosphere (20 % O_2 and 80 % N_2). Samples were placed in an alumina crucible and heated at a rate of 10 °C/min. For both XRD and DSC analyses, the glass samples were crushed in an agate mortar, sieved, and the resulting powders with a granulometry of 150–250 μm were selected.

2.4. Density measurements

The density of all glass samples was measured using the Archimedes displacement method, with water as the immersion liquid. Measurements were performed using a digital balance with an accuracy of ±0.1 mg, and each experiment was repeated five times to ensure reliability. The percentage error in the measurement of density was ±0.05 %.

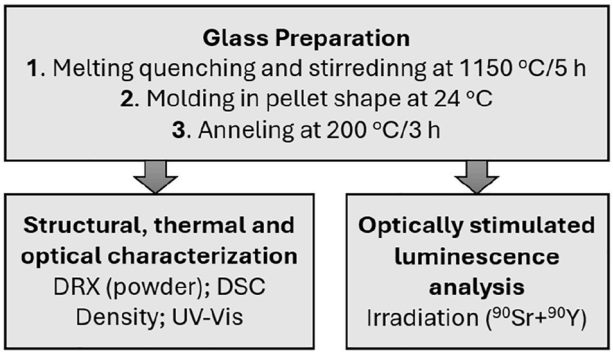

Fig. 1. The main analytical steps performed in the preparation and characterization of glass samples.

Table 1
Physical properties of the 80MBO and 60MBO samples. $<d_{B\text{-}B}>$ is the average boron-boron separation.

Glass	Density (g/cm^3) ± 0.05	Molecular weight (gmol^{-1})	Molar volume (cm^{3}mol^{-1})	Ion concentration (Nx10^{22} ion cm^{-3})	Polaron Radius, r_p (Å)	Inter-nuclear distance, r_i (Å)	$<d_{B\text{-}B}>$ (nm)	Field strength (F), F·10^{17} (cm^2)
80MBO	2.19	103.20	47.12	–	–	–	3.61	–
80MBO:0.1Ce	2.49	103.24	41.46	0.14	3.55	8.83	3.47	0.45
80MBO:0.3Ce	2.50	103.30	41.32	0.43	2.46	6.12	346	0.95
80MBO:0.5Ce	2.51	103.37	41.18	0.73	2.08	5.15	3.45	1.34
80MBO:0.7Ce	2.52	103.43	41.04	1.03	1.85	4.60	3.45	1.69
80MBO:0.9Ce	2.53	103.50	40.91	1.32	1.70	4.23	3.44	1.99
60MBO	1.49	98.40	66.04	–	–	–	4.04	–
60MBO:0.1Ce	1.96	98.44	53.21	0.11	3.86	9.59	3.76	0.38
60MBO:0.3Ce	1.97	98.50	51.30	0.35	2.64	6.57	3.71	0.82
60MBO:0.5Ce	1.98	98.57	50.54	0.59	2.22	5.51	3.69	1.17
60MBO:0.7Ce	1.99	98.63	49.81	0.84	1.98	4.91	3.68	1.48
60MBO:0.9Ce	2.00	98.70	49.35	1.09	1.81	4.49	3.67	1.76

2.5. Optical and luminescence characterization

Absorption spectra were recorded using a Shimadzu UV–VIS–NIR spectrophotometer (model UV-1800, double-beam). The optical band gaps were calculated for direct and indirect transitions from the absorption data. Photoluminescence spectra were acquired at room temperature using a Jasco FP-8600 spectrofluorophotometer equipped with a xenon light source.

2.6. OSL measurements

OSL measurements were carried out at room temperature in an automated Risø TL/OSL reader (model DA-20, DTU Nutech). The OSL signal was stimulated in CW mode using blue LEDs (470 nm, FWHM = 20 nm) delivering a maximum power density of 80 mW/cm^2 at the sample position. The emitted OSL signal was detected by a bialkali photomultiplier tube behind a UV-transmitting visible-absorbing filter (Hoya U-340, 7.5 mm thickness) to block the stimulation light while transmitting the ultraviolet part (ca. 250–400 nm) of the OSL signal and a 2 mm diameter mask. The samples were irradiated with a ^{90}Sr/^{90}Y beta source from the TL/OSL reader, delivering a dose rate of 10 mGy/s. The samples were exposed to absorbed doses in the range of 20 mGy to 5 Gy.

3. Results and discussion

3.1. Structural analysis

The undoped and doped 80MBO and 60MBO glasses synthesized in this work are shown in Fig. 2. The undoped samples are colorless, while those doped with Ce exhibit a yellowish hue, attributed to cerium's incorporation into the glass matrix. The XRD pattern of the prepared samples, presented in Fig. 3, confirms the predominantly amorphous nature of the prepared samples. However, the undoped glasses exhibit a sharp peak at $2\theta = 26.6^o$ (Fig. 3a and b), suggesting the presence of crystalline $Mg_2B_2O_5$ (Liu et al., 2019). This peak, observed in the middle of the melting process, corresponds to the phase diagram of the B_2O_3-MgO system under the glass synthesis conditions at 1150 °C (Mutluer and Timucin, 1975). The introduction of Ce doping, however, suppresses the formation of Mg_2B_2O5, as evidenced by the absence of the $2\theta = 26.6^o$ sharp peak in the XRD patterns of doped glasses. This suppression is likely due to an increase in structural disorder induced by the dopant, which prevents crystallization. Thus, only the amorphous phase characteristic of borate glasses is seen in the XRD diffractogram of the doped glasses, highlighting the effectiveness of Ce doping in promoting glass homogeneity.

With the addition of ions Ce^{3+} in glasses, the XRD spectrum shows the absence of intense peaks related to residual orders in the structure. This indicates that the incorporation of the dopant Ce^{3+}, which has a higher atomic number than the other constituent elements, induces significant structural modifications in the glass's matrix. These structural changes are corroborated by the observed increase in glass densities and reduction in molar volumes (Table 1). The density of the 80MBO:0.9Ce glass is 15 % higher than that of non-doped glass. Likewise, the comparison between the density of the undoped MBO glass and that of the doped samples confirms an increase in density of up to 35 %. For the 80MBO samples, a reduction of up to 13.2 % was observed, while for the 60MBO samples, the molar volume decreased by up to 25 %. These reductions in molar volume indicate a higher degree of structural compaction in the doped glasses, likely due to the enhanced network connectivity facilitated by the incorporation of Ce^{3+} ions. This compaction is consistent with the increased density values and further supports the role of Ce^{3+} as a modifier that disrupts residual crystallinity and enhances the amorphous nature of the glass structure.

The physical properties of the synthesized samples are summarized in Table 1. The calculation of these properties followed the formalism described by Mhareb et al. (2015). As expected, the molecular weight, ion concentrations, and average boron-boron separation ($<d_{B\text{-}B}>$) of the samples increased as a function of the dopant concentration in both glass matrices.

Table 1 also shows a considerable decrease in the inter-nuclear distance and the polaron radius with increasing dopant concentration in both 80MBO and 60MBO glasses. These changes can be attributed to the higher concentration of Ce^{3+} ions within the glass matrix. Consequently, the significant enhancement in the field strengths is due to the occurrence of strong bonds between the Ce^{3+} and B^- ions. This type of bond is attributed to the possible displacement between the Ce^{3+} and newly generated oxygen atoms from the conversion of BO_3–BO_4 units (Zaman et al., 2017).

Fig. 4 shows the differential scanning calorimetry (DSC) thermograms of the glasses under investigation. All the thermograms exhibit a slight endothermic effect between 550 °C and 650 °C, which corresponds to the glass transition temperature (Tg). At higher temperatures, an exothermic peak (Tc) is observed related to the beginning of the crystallization process, followed by another endothermic effect due to the re-melting of the glass, symbolized by Tm. The data shows that Tg increases similarly with growth in compactness of structure, consistent with the densification of the matrix due to Ce^{3+} doping. A brief summary of the DSC parameters of these glasses is presented in Table 2. An analysis of the stability parameter $(T_c\text{-}T_g)/T_m$ shows variation between the different glasses' matrices. The 60MBO matrix demonstrates greater thermal stability compared to the 80MBO glass. Furthermore, an increase in thermal stability was observed with higher Ce^{3+} content in both matrices. This result suggests that adding the Ce^{3+} dopant enhances the overall stability of the glass structure, as also noted by Subbalakshmi and Veeraiah (2002).

3.2. Optical absorption and photoluminescence analysis

Fig. 5 illustrates dependence of $(\alpha h\nu)^{½}$ and $(\alpha h\nu)^2$ on photon energy ($h\nu$) for different Ce^{3+} ion concentrations. The optical band gap (Eg) of glass was calculated using equation (1).

$$\alpha h\nu = B(h\nu - Eg)^n \quad (1)$$

where α is the absorption coefficient, $h\nu$ is the incident photon energy, B is a constant, and the n value is 2 for indirect allowed and 1/2 for direct allowed transition (Wantana et al., 2018). The calculated values of

Fig. 2. Pellets of 80MBO and 60MBO; (a) a pellet glass, (b) undoped, and (c) Ce^{3+} doped.

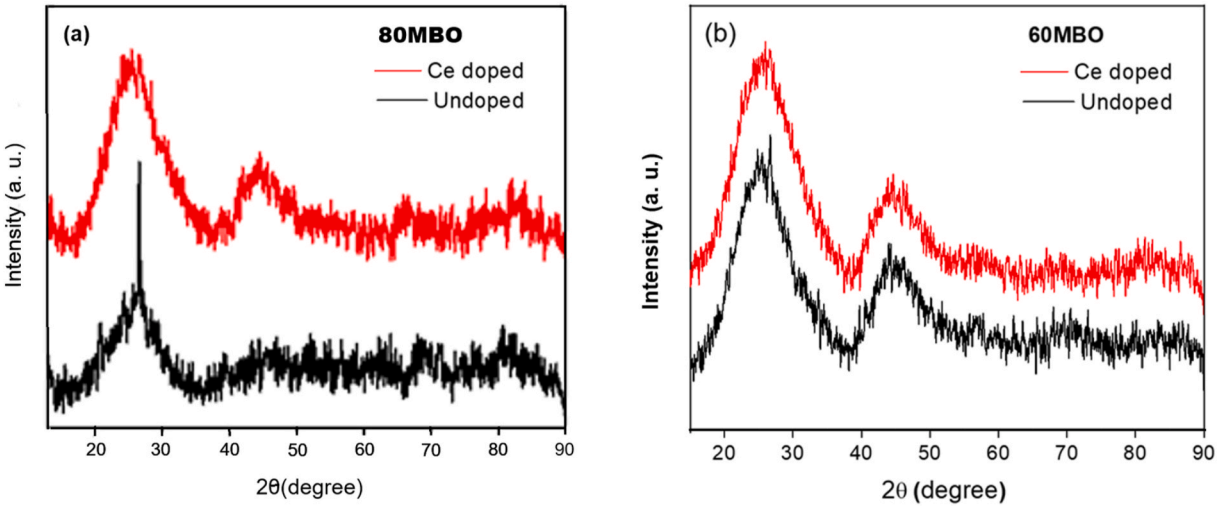

Fig. 3. X-ray diffraction patterns of undoped and Ce-doped 80MBO and 60MBO glass samples.

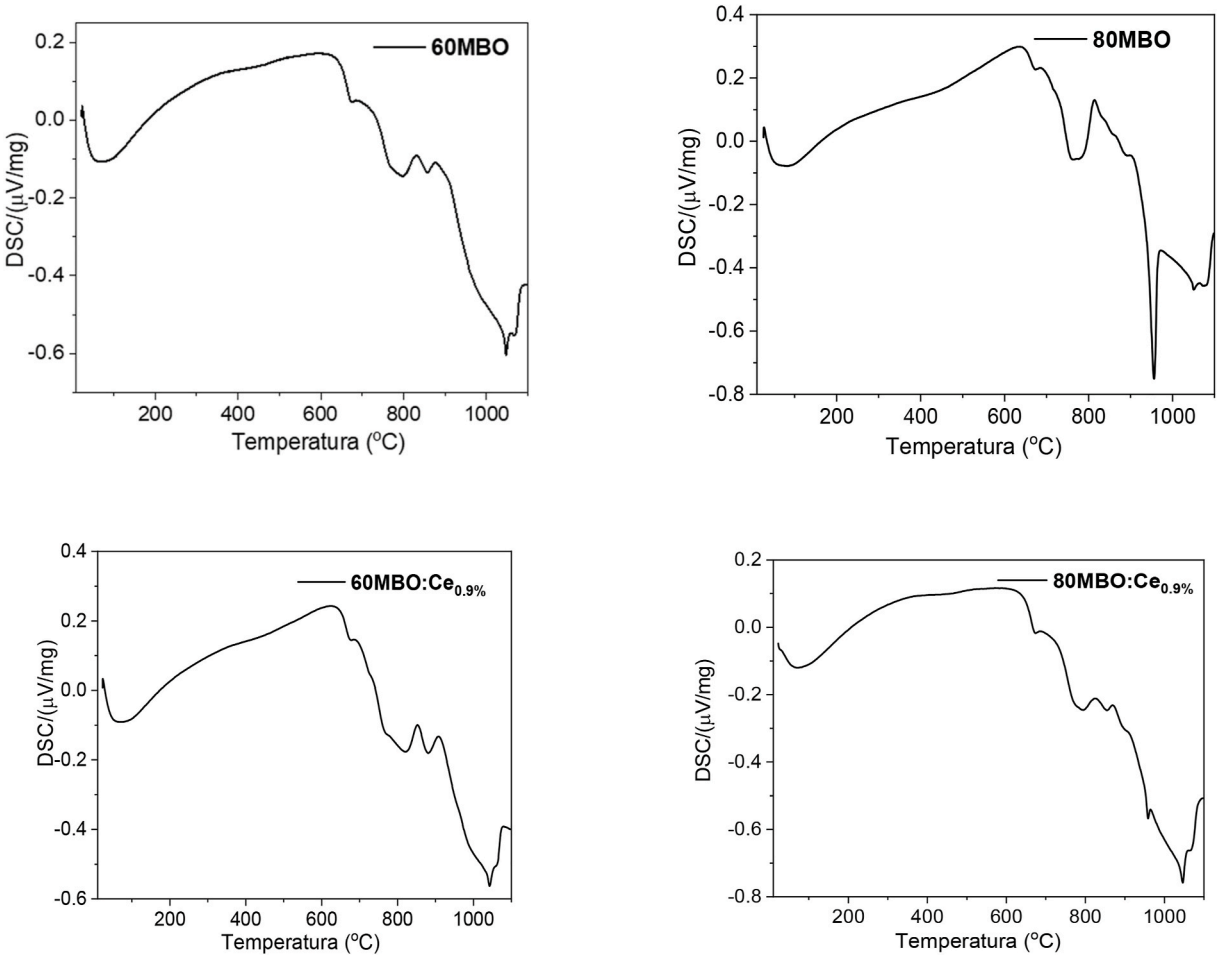

Fig. 4. DSC curves for 80MBO, 60MBO, 80MBO:0.9Ce, and 60MBO:0.9Ce glasses.

direct and indirect band gap energies, varies in the range of 3.14–2.42 eV (Figs. 5a) and 3.55–3.61 eV (Fig. 5b) for the 80MBO samples; 3.36–2.63 eV (Figs. 5c) and 3.90–3.35 eV (Fig. 5d) for the 60MBO samples, respectively. Table 3 summarizes the indirect and direct band gaps of the undoped and doped glasses. The reduction of the optical band gap with the addition of Ce^{3+} is attributed to the structural modifications within the glass network (Choi and RyuBong, 2015; Wantana et al., 2018). As the Ce^{3+} content increases, defects in the charge distribution around oxygen ions become more pronounced, leading to a higher degree of localization. These localized negative charges surrounding Ce^{3+} induce the 4f shell of the Ce^{3+} ion to get closer to the 5d shell. This approximation shifts the 4f-5d transition energy to the lower energy side and increases the cut-off wavelength in the absorption spectra (Bahadur et al., 2013). In view of this, it appears that the 60MBO

Table 2
Summary of DSC parameter results of pure and 0.9Ce-doped glasses.

Glass	T_g (±2 °C)	T_c (±2 °C)	T_m (±2 °C)	$(T_c-T_g)/T_m$
80MBO	636	814	956	0.186
60MBO	594	832 880	1047	0.227
80MBO:0.9Ce	626	828 868	1047	0.193
60MBO:0.9Ce	622	908	1031	0.277

matrix remains with a greater gap than the 80MBO matrix. This suggests that the 60MBO matrix experiences less structural disruption with the incorporation of Ce^{3+} ions, maintaining a relatively wider energy gap.

Fig. 6 shows the excitation and emission spectra of the 80MBO:Ce and 60MBO glasses. The samples were excited with 250 nm, corresponding to the 5d – 4f transition of Ce^{3+} ions (Wantana et al., 2018). For the 80MBO:Ce glasses, the maximum emission bands are observed between 357 nm and 390 nm (Fig. 6a). For the 60MBO:Ce glasses, the emission bands have maximum intensities between 357 nm and 385 nm. However, it is possible to observe the predominance of two sites, promoting two superimposed peaks that are best seen in the excitation spectrum for both 80MBO:Ce and 60MBO:Ce, with bands centered around 270 nm and 310 nm. These excitation sites induce a broadening of the emission band and the displacement of the centers of maximum intensity due to excitation of both levels of the sites that are the Ce^{3+} ions (Bahadur et al., 2013). It should be noted that both matrices show a low intensity emission from 350 nm to 490 nm, even in the samples with the highest concentration of Ce^{3+} ions. In the region of characteristic host emission, there is an increase in the intensity of emission, which is possibly evidence of energy transfer between the matrix and Ce^{3+} ions.

3.3. Optically stimulated luminescence analysis

OSL decay curves for undoped and Ce-doped 80MBO and 60MBO glasses irradiated with 1.0 Gy are shown in Fig. 7. Both undoped glasses exhibit extremely low OSL signals compared to the doped glasses. However, the undoped 80MBO glass shows a better OSL response than 60MBO, indicating minor intrinsic differences in trap density or recombination dynamics between the two matrices. The 60MBO:Ce samples show a better OSL response than the doped 80MBO glasses. However, as the concentration of cerium increases, the signal response

Table 3
Indirect and direct band gap of the undoped and doped glasses.

% Ce	80MBO		60MBO	
	Direct energy gap (eV)	Indirect energy gap (eV)	Direct energy gap (eV)	Indirect energy gap (eV)
0	3.14	3.83	3.36	3.90
0.1	2.88	3.61	2.78	3.26
0.3	2.77	3.44	2.98	3.52
0.5	2.68	3.44	2.98	3.52
0.7	2.58	3.32	2.78	3.26
0.9	2.42	3.24	2.63	3.35

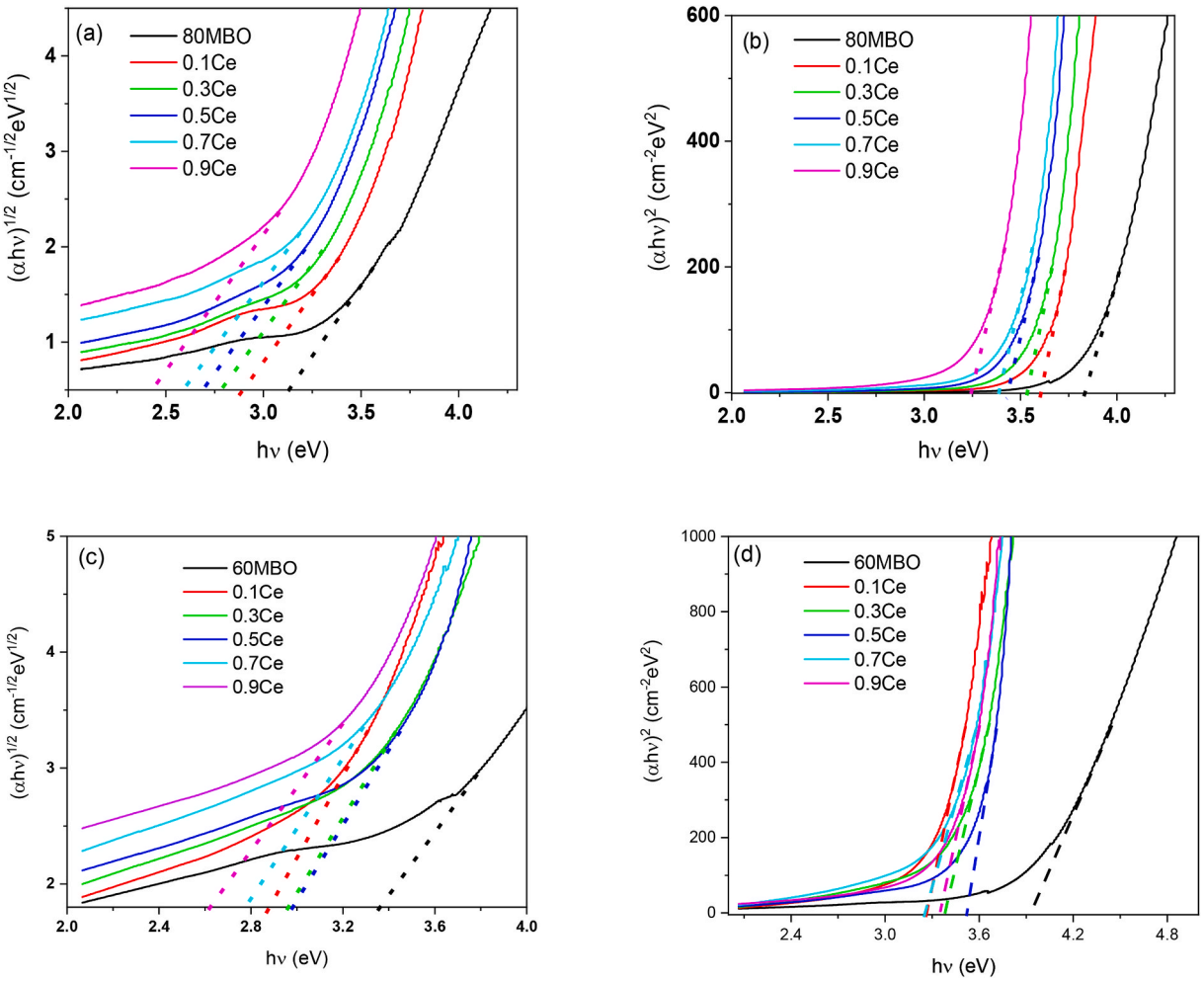

Fig. 5. The Tauc plot for the (a) direct and (b) indirect band gap of 80MBO:Ce samples, (c) direct and (d) indirect band gap of 60MBO:Ce samples.

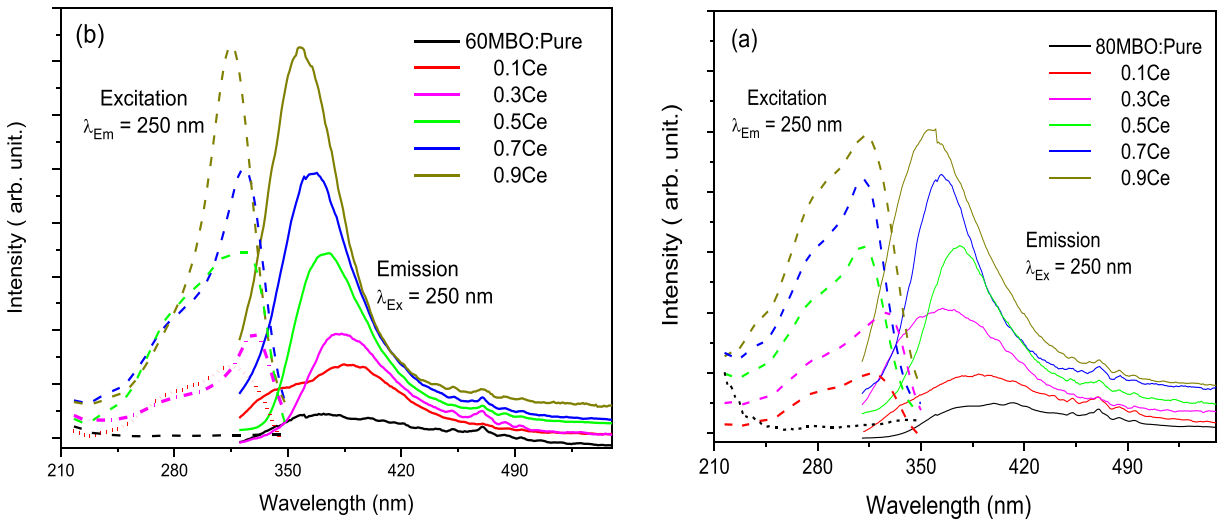

Fig. 6. (a) The excitation (dashed line) and emission (solid line) spectra under Ce^{3+} ions in 80MBO and (b) 60MBO glass samples.

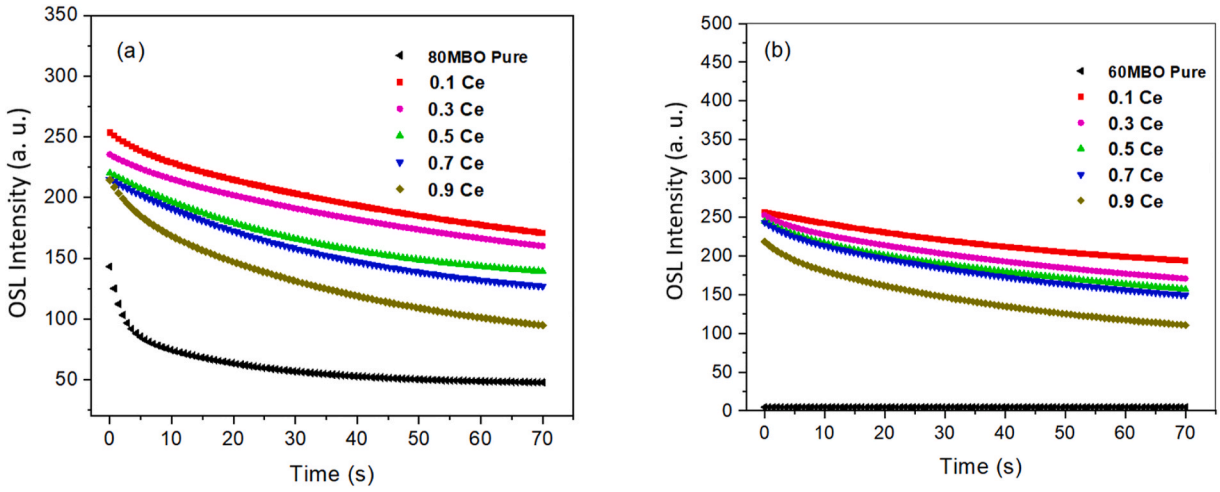

Fig. 7. OSL decay curves for (a) 80MBO:Ce and (b) 60MBO:Ce at a dose of 1.0 Gy.

decreases for both matrices. This reduction is due to the higher abundance of Ce^{3+} ions in the 80MBO and 60MBO glasses, which can act as strong deactivator sites of luminescence recombination centers, i.e., the electron-hole pairs can then relax through defect traps, non-radiative recombination on the excited centers.

To analyze this response, the decaying OSL curve was integrated over the whole time interval until the signal stabilization, with the background noise and the offset due to the stimulating LED subtracted. Fig. 8 shows the dependence behavior of the OSL area (OSL response) as a function of the absorbed dose for the different concentrations of Ce^{3+} in the two glass hosts. The area under the OSL curves as a function of absorbed dose for the undoped glasses was excluded from this analysis due to their weak OSL intensity. Although rare-earth dopants provide alternative hole traps, and therefore luminescence centers, a higher concentration of Ce^{3+} leads to a higher probability of non-radiative recombination, reducing the overall OSL intensity (Kalnins et al., 2011). This trend is consistent with the observations in Fig. 7, where the OSL signal decreases with increasing Ce^{3+} content, and Fig. 8, where the integrated OSL area decreases correspondingly for higher concentrations of Ce^{3+}.

In Fig. 8c, the dose-responses of 80MBO:0.9Ce and 60MBO:0.9Ce glasses were adjusted using linear and exponential functions with respect to radiation dose in the 0.02–5 Gy range, yielding R^2 values of 0.9972 and 0.9999, respectively. These high correlation coefficients demonstrate the potential suitability of these glasses for dosimeter applications. Although the data visually suggests a linear relationship, the exponential fit provides a more accurate dose prediction model. This is particularly relevant at higher absorbed doses, where the response behavior begins to saturate, as reported in the literature (Kalnins et al., 2011). This saturation effect is attributed to the filling of all electron or hole traps in the material, beyond which further irradiation does not increase the population of trapped charges (Kalnins et al., 2011; Al Helou et al., 2018).

Fig. 9 illustrates the fading phenomenon of the OSL signal for a dose of 1.0 Gy. Measurements were taken immediately after exposure to beta radiation, and the same sample was irradiated again a week later for a second OSL reading. A fading of 65 % was observed, highlighting the importance of signal stability - a critical criterion in dosimetry applications. At room temperature, trapped carriers can be thermally released from defect traps to undergo recombination, thus reducing the anticipated signal related to the number of trapped carriers (Al Helou et al., 2018). The observed fast fading suggests that the material may experience significant signal loss over time. Further investigation into the long-term fading curve will be conducted in future studies to understand the stability and performance of the optical material for dosimetric applications.

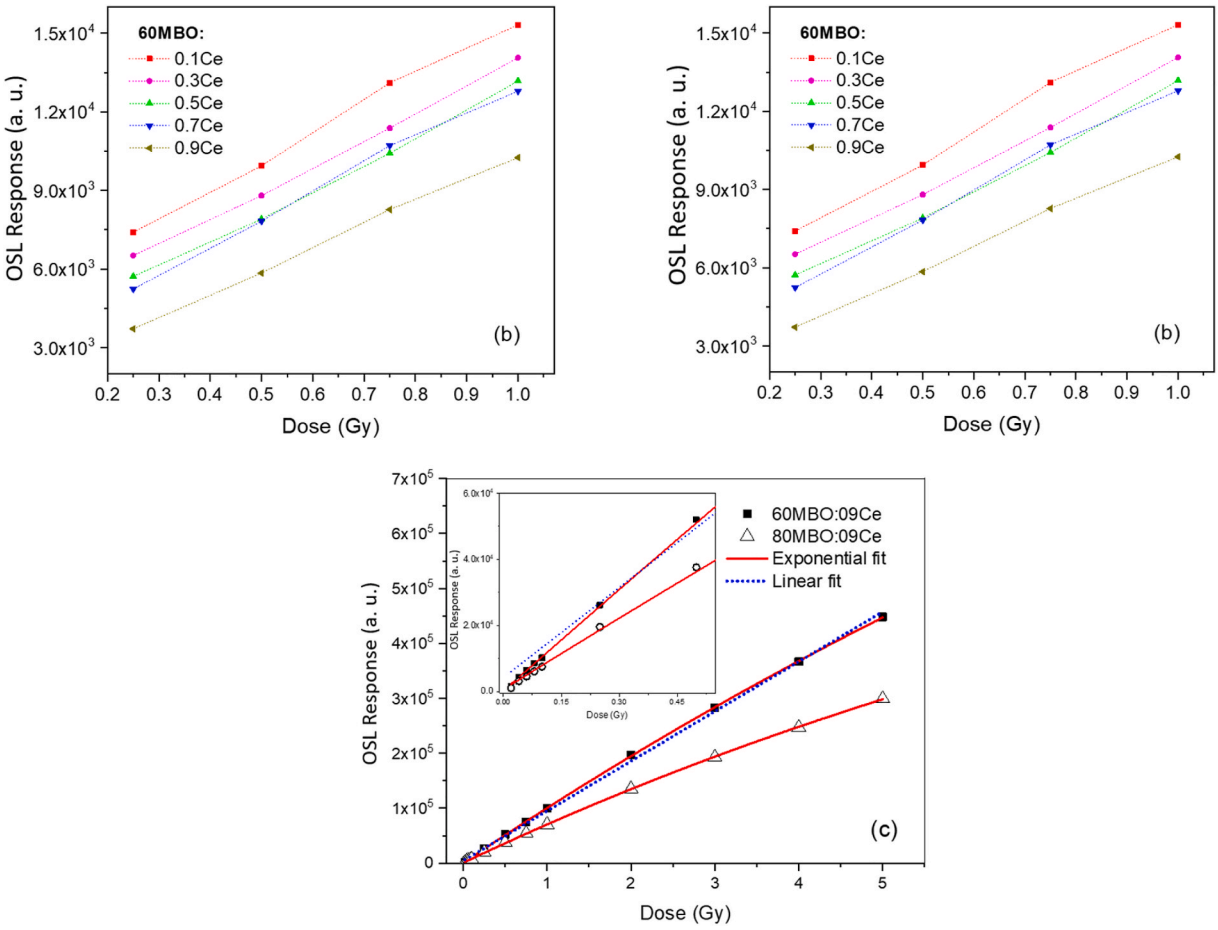

Fig. 8. OSL dose-response curve of (a) 80MBO:Ce and (b) 60MBO:Ce samples for different doses of 0.25–1.0 Gy. (c) OSL dose response curve of 80MBO:0.9Ce and 60MBO:0.9Ce samples for different doses of 0.02–5.0 Gy. The red solid line is the exponential fit, and the blue solid line is the linear fit. The inset shows the dose response curve for the low dose range (0.02–0.5 Gy). (For interpretation of the references to color in this figure legend, the reader is referred to the Web version of this article.)

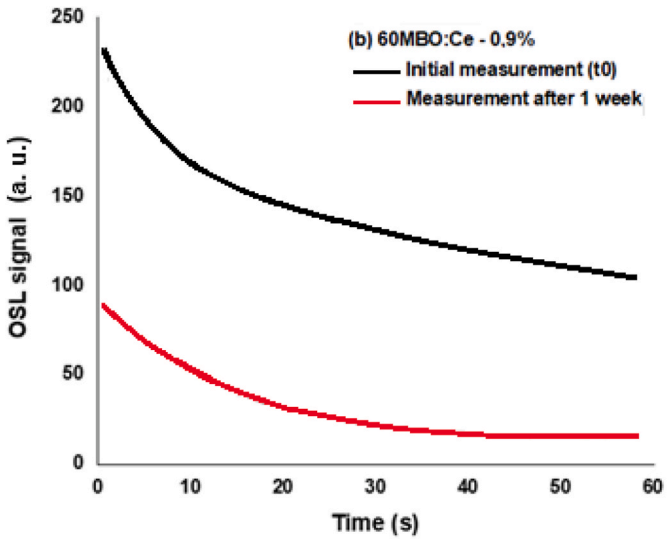

Fig. 9. Fading of the OSL signal with time at room temperature.

4. Conclusion

The influence of Ce^{3+} ions on the physical and optical properties of 80MBO and 60MBO glasses prepared by the conventional melt-quenching method was systematically studied. The XRD measurements confirm the amorphous nature of glass and a possible trace of crystal residue in the system that disappears upon doping with Ce ions. These structural changes were further corroborated by the calculated values of average boron-boron separation. A decrease in molar volumes and an increase in glass density were observed with Ce doping, indicating compaction in the glass network. The glasses exhibited absorption of photons in the UV and visible region. At the same time, the indirect and direct band gap energies decreased with the increment of Ce^{3+} content, due to structural changes and reduction in molar volume. The Ce^{3+} excitation spectra show the predominance of two sites, promoting two superimposed peaks centered around 270 nm and 310 nm. The emission spectra demonstrated strong bands of emission corresponding to the Ce^{3+} 5d – 4f transitions, with a broadening and a shift of emission peaks toward shorter wavelengths, indicating changes in the luminescence characteristics with doping. Undoped glasses exhibited a low OSL response, while cerium-doped glasses showed significantly stronger OSL signals. Among the doped glasses, those with 0.1 % of Ce^{3+} concentration produced the highest OSL response, likely due to the greater population of metastable electron-hole pairs. In contrast, higher Ce^{3+} concentrations reduced the OSL response due to the increased presence of luminescence quenching centers. The dose-response curve demonstrated a better fit with an exponential model across the studied dose range (0.02–5.0 Gy), providing a predictive model for dose measurements, especially at higher doses where saturation effects become evident. Finally, the glasses exhibited a fast fading, with the OSL signal decreasing by 65 % one week after irradiation. This significant fading

indicates the need for further studies to improve the long-term stability of the OSL signal, which is critical for reliable dosimetric applications.

CRediT authorship contribution statement

Gerardo R. Barrera: Writing – original draft, Investigation, Formal analysis, Data curation, Conceptualization. **Adriel S. Almeida:** Investigation, Formal analysis. **Bruno M. Vidigal:** Investigation. **Anderson M.B. Silva:** Writing – review & editing, Formal analysis. **Matheus C.S. Nunes:** Investigation. **Andrea L.F. Novais:** Investigation. **Neilo M. Trindade:** Writing – review & editing, Investigation. **Divanizia N. Souza:** Writing – review & editing, Supervision, Project administration.

Declaration of competing interest

The authors declare that they have no known competing financial interests or personal relationships that could have appeared to influence the work reported in this paper.

Acknowledgments

The authors thank the Brazilian agencies Comissão Nacional de Energia Nuclear (CNEN), Coordenação de Aperfeiçoamento de Pessoal de Nível Superior - CAPES and Conselho Nacional de Desenvolvimento Científico e Tecnológico - CNPq (Projects: 307008/2022–3, 407493/2021–2, 406761/2022–1 - National Institute of Radiation Technology in Health Science (INTERAS). A.M.B. Silva thanks FAPESP for financial support (#2023/04859–8); M.C.S. Nunes personally acknowledges funding by FAPESP (#2021/12758–1; #2022/14516–8) and N.M. Trindade thanks FAPESP (#2018/05982–0; #2019/05915–3; #2024/03006–4) and CNPq (#444110/2024–0; #409338/2021–4; #306929/2022–8).

Data availability

Data will be made available on request.

References

Al Helou, N., El Hamzaoui, H., Capoen, B., Bouwmans, G., Cassez, A., Ouerdane, Y., Bouazaoui, M., 2018. Radioluminescence and optically stimulated luminescence responses of a cerium-doped sol-gel silica glass under X-ray beam irradiation. IEEE Trans. Nucl. Sci. 65 (8), 1591–1597. https://doi.org/10.1109/tns.2017.2787039.

Bahadur, A., Dwivedi, Y., Rai, S.B., 2013. Optical properties of cerium doped oxyfluoroborate glass. Spectrochim. Acta Mol. Biomol. Spectrosc. 110, 400–403. https://doi.org/10.1016/j.saa.2013.03.066.

Barrera, G.R., Souza, L.F., Novais, A.L.F., Caldas, L.V.E., Abreu, C.M., Machado, R., Souza, D.N., 2018. Thermoluminescence and optically stimulated luminescence of PbO–H_3 BO_3 and PbO–H_3BO_3–Al_2O_3 glasses. Radiat. Phys. Chem. https://doi.org/10.1016/j.radphyschem.2018.02.005.

Choi, S.Y., RyuBong, B.K., 2015. Optical, structural, and thermal properties of ceriumdoped zinc borophosphate glasses. J. Nanosci. Nanotechnol. 15 (11), 8756–8762. https://doi.org/10.1166/jnn.2015.11550.

Feitosa, C.A.C., 2004. Synthesis, Crystallization, and Characterization of Glasses in the TiO_2-BaO-B_2o_3 System. Institute of Physics of São Carlos, University of São Paulo, São Carlos, p. 187, 2004. Ph.D. Thesis.

Kalnins, C.A.G., Ebendorff-Heidepriem, H., Spooner, N.A., Monro, T.M., 2011. Optically stimulated luminescence in fluoride-phosphate glass for radiation dosimetry. J. Am. Ceram. Soc. 94 (2), 474–477. https://doi.org/10.1111/j.1551-2916.2010.04231.x.

Kawano, N., Kawaguchi, N., Okada, G., Fujimoto, Y., Yanagida, T., 2018. Scintillation and dosimetric properties of Ce-doped strontium aluminoborate glasses. J. Non-Cryst. Solids 482, 154–159. https://doi.org/10.1016/j.jnoncrysol.2017.12.030.

Lim, T.Y., Wagiran, H., Hussin, R., Hashim, S., Saeed, M.A., 2014. Physical and optical properties of Dysprosium ion doped borate glasses. Phys. B. 451, 63–67. https://doi.org/10.1016/j.physb.2014.06.028.

Liu, Y., Jiang, T., Huang, W., Liu, C., Wang, J., Xue, X., 2019. High temperature dielectric properties of ludwigite and its effect on microwave heating process. J. Microw. Power Electromagn. Energy 53 (3), 195–211. https://doi.org/10.1080/08327823.2019.1643650.

McKeever, S.W.S., 1988. Thermoluminescence of Solids. Cambridge University Press, Cambridge.

Mhareb, M.H.A., Hashim, S., Ghoshal, S.K., Alajerami, Y.S.M., Saleh, M.A., Azizan, S.A. B., Karim, M.A., 2015. Influences of dysprosium and phosphorous oxides codoping on thermoluminescence features and kinetic parameters of lithium magnesium borate glass. J. Radioanal. Nucl. Chem. 305, 469–477. https://doi.org/10.1007/s10967-015-3984-x.

Mutluer, T., Timucin, M., 1975. Phase equilibria in the system MgO–B_2O_3. J. Am. Ceram. Soc. 58 (5/6), 196–197. https://doi.org/10.1111/j.1151-2916.1975.tb11442.x.

Okada, G., Morrell, B., Koughia, C., Edgar, A., Varoy, C., Belev, G., Kasap, S., 2011. Spatially resolved measurement of high doses in microbeam radiation therapy using samarium doped fluorophosphate glasses. Appl. Phys. Lett. 99 (12), 121105. https://doi.org/10.1063/1.3633102.

Okada, G., Kasap, S., Yanagida, T., 2016. Optically- and thermally-stimulated luminescences of Ce-doped SiO_2 glasses prepared by spark plasma sintering. Opt. Mater. 61, 15–20. https://doi.org/10.1016/j.optmat.2016.08.020.

Rowlands, J.A., 2002. The physics of computed radiography. Phys. Med. Biol. 47, R123. https://doi.org/10.1088/0031-9155/47/23/201.

Silva, A.M.B., Jesus, L.S., Correa, W., Junot, D.O., Caldas, L.V.E., Dantas, N.O., Silva, A. C., 2023. Luminescence characterization of BioGlass undoped and doped with europium and silver ions. Appl. Radiat. Isot. 201, 110997. https://doi.org/10.1016/j.apradiso.2023.110997.

Souza, L.F., Antonio, P.L., Caldas, L.V.E., Souza, D.N., 2015. Neodymium as a magnesium tetraborate matrix dopant and its applicability in dosimetry and as a temperature sensor. Nuclear Instruments & Methods in Physics Research Section A-Accelerators Spectrometers Detectors and Associated Equipment 784, 9–13. https://doi.org/10.1016/j.nima.2014.12.030.

Subbalakshmi, P., Veeraiah, N., 2002. Study of CaO–WO_3–P_2O_5 glass system by dielectric properties, IR spectra and differential thermal analysis. J. Non-Cryst. Solids 298 (1), 89–98. https://doi.org/10.1016/s0022-3093(01)01039-0.

Tatsumi, H., Okada, G., Yanagida, T., Masai, H., 2016. Scintillation and dosimeter properties of Ce-doped Li3PO4–Al(PO3)3 glasses. J. Ceram. Soc. Jpn. 124 (5), 550–553. https://doi.org/10.2109/jcersj2.15231.

Wantana, N., Kaewnuam, E., Chanthima, N., Kaewjaeng, S., Kim, H.J., Kaewkhao, J., 2018. Ce^{3+} doped glass for radiation detection material. Ceram. Int. https://doi.org/10.1016/j.ceramint.2018.08.121.

Yanagida, T., Kato, T., Nakauchi, D., Kawaguchi, N., 2022. Fundamental aspects, recent progress and future prospects of inorganic scintillators. Jpn. J. Appl. Phys. 62 (1), 10508.

Yukihara, E.G., McKeever, S.W.S., 2011. Optically Stimulated Luminescence. John Wiley Sons, Ltd, Chichester, UK. https://doi.org/10.1002/9780470977064.

Zaman, F., Rooh, G., Srisittipokakun, N., Kim, H.J., Kaewnuam, E., Meejitpaisan, P., Kaewkhao, J., 2017. Scintillation and luminescence characteristics of Ce $^{3+}$ doped in Li_2 O–Gd $_2$ O_3 –BaO–B_2O_3 scintillating glasses. Radiat. Phys. Chem. 130, 158–163. https://doi.org/10.1016/j.radphyschem.2016.08.016.